



# Investigation of phases in $\text{Al}_{23}\text{Co}_{15}\text{Cr}_{23}\text{Cu}_8\text{Fe}_{15}\text{Ni}_{16}$ and $\text{Al}_8\text{Co}_{17}\text{Cr}_{17}\text{Cu}_8\text{Fe}_{17}\text{Ni}_{33}$ high entropy alloys and comparison with equilibrium phases predicted by Thermo-Calc

A. Manzoni<sup>a,\*</sup>, H. Daoud<sup>b</sup>, S. Mondal<sup>c</sup>, S. van Smaalen<sup>c</sup>, R. Völkl<sup>b</sup>, U. Glatzel<sup>b</sup>, N. Wanderka<sup>a</sup>

<sup>a</sup> Helmholtz-Zentrum Berlin für Materialien und Energie, Hahn-Meitner-Platz 1, D-14109 Berlin, Germany

<sup>b</sup> Metals and Alloys, University Bayreuth, Ludwig-Thoma-Str. 36b, D-95447 Bayreuth, Germany

<sup>c</sup> Crystallography, University Bayreuth, Universitätsstr. 30, D-95440 Bayreuth, Germany

## ARTICLE INFO

### Article history:

Received 18 July 2012

Received in revised form 31 October 2012

Accepted 2 November 2012

Available online 19 November 2012

### Keywords:

High entropy alloys

Microstructure

Transmission electron microscopy

Atom probe tomography

## ABSTRACT

$\text{Al}_{23}\text{Co}_{15}\text{Cr}_{23}\text{Cu}_8\text{Fe}_{15}\text{Ni}_{16}$  and  $\text{Al}_8\text{Co}_{17}\text{Cr}_{17}\text{Cu}_8\text{Fe}_{17}\text{Ni}_{33}$  high entropy alloys were investigated by scanning electron microscopy, transmission electron microscopy and three dimensional atom probe. While the brittle  $\text{Al}_{23}\text{Co}_{15}\text{Cr}_{23}\text{Cu}_8\text{Fe}_{15}\text{Ni}_{16}$  alloy decomposes during solidification mainly into two body centred cubic phases, the ductile  $\text{Al}_8\text{Co}_{17}\text{Cr}_{17}\text{Cu}_8\text{Fe}_{17}\text{Ni}_{33}$  shows two prominent face-centred cubic phases.  $\text{Al}_{23}\text{Co}_{15}\text{Cr}_{23}\text{Cu}_8\text{Fe}_{15}\text{Ni}_{16}$  consists of Fe–Cr-rich and Cu-rich intermetallic phases embedded in an Al–Ni-rich solid solution matrix. The microstructure of  $\text{Al}_8\text{Co}_{17}\text{Cr}_{17}\text{Cu}_8\text{Fe}_{17}\text{Ni}_{33}$  is mainly characterized by two phases. Nano-sized precipitates enriched mainly in Ni are embedded in a matrix depleted in Al and Cu. The phases observed in both high entropy alloys are compared with the equilibrium phases predicted by Thermo-Calc simulation.

© 2012 Elsevier B.V. All rights reserved.

## 1. Introduction

High entropy alloys have been known as a new type of materials and have been defined as having five or more principal elements, each one having a concentration between 5 and 35 at.%. [1–3]. They are crystalline materials which predominantly may form simple solid solutions, mainly of face-centred cubic (fcc) or body-centred cubic (bcc) structure. The general absence of a single base element distinguishes them from alloys based on one principal element with a content of up to 80 wt.% or more [4,5]. High entropy alloys promise an interesting combination of properties, such as oxidation resistance, thermal stability, high strength and soft magnetic behaviour. [3,6–9].

The most studied high entropy alloy is AlCoCrCuFeNi with equiatomic composition [4,5,10,11]. This high entropy alloy solidifies dendritically within wide casting conditions. The dendrites mainly consist of two phases, an Al–Ni-rich and a Fe–Cr-rich phase, whereas interdendritic regions are enriched in Cu [4,10]. It has also been found that the Fe–Cr-rich phase decomposes into Fe-rich and Cr-rich domains. A length scale between these domains of just a few nanometres indicates spinodal decomposition as the formation process [8], which is often observed in Fe–Cr systems [12,13]. In addition, several types of Cu-rich precipitates, differentiated by

their morphologies, have been observed within the Al–Ni matrix [10]. Furthermore, the microstructure of  $\text{Al}_x\text{CoCrCuFeNi}$  is very sensitive to the Al level in the high entropy alloy. While alloys with an Al content less than  $x = 0.5$  are composed of a simple solid solution with a fcc structure, a mixtures of fcc and bcc phases have been observed in the alloys with  $x \geq 0.8$  and finally at  $x = 2.8$  and higher a simple bcc ordered structures were obtained [5]. Mechanical properties of high entropy alloys are correlated to their microstructures. An increase of the Al content in the  $\text{Al}_x\text{CoCrCuFeNi}$  alloy provokes multi phase microstructure which results in a hardness increase [3,11]. However, alloys with high Al contents are more brittle [5,11].

In order to optimize the behaviour of high entropy alloys at high-temperatures for structural and functional applications, the knowledge of the microstructure and phase composition of a material is essential for the understanding and prediction of its macroscopic mechanical properties. The first step of this work therefore was to investigate the microstructure of selected alloys on the micro and nano scale. The concept was to modify the composition of equiatomic AlCoCrCuFeNi alloy in order to reduce the number of phases in the alloy. Hence two alloys with different Al and Ni composition and reduced Cu content,  $\text{Al}_{23}\text{Co}_{15}\text{Cr}_{23}\text{Cu}_8\text{Fe}_{15}\text{Ni}_{16}$  and  $\text{Al}_8\text{Co}_{17}\text{Cr}_{17}\text{Cu}_8\text{Fe}_{17}\text{Ni}_{33}$ , were selected. The work has focused on microstructure investigations. X-ray diffraction (XRD), transmission electron microscopy (TEM) and three-dimensional atom probe (3D-AP) were used for this study. The phase characterization using

\* Corresponding author. Tel.: +49 30 8062 42326; fax: +49 30 8062 43059.

E-mail address: [anna.manzoni@helmholtz-berlin.de](mailto:anna.manzoni@helmholtz-berlin.de) (A. Manzoni).

3D-AP analysis is combined with thermodynamic calculations using Thermo-Calc [14]. The observed phases in as-cast alloys are compared with the equilibrium phases predicted by Thermo-Calc.

## 2. Experimental

$\text{Al}_{23}\text{Co}_{15}\text{Cr}_{23}\text{Cu}_8\text{Fe}_{15}\text{Ni}_{16}$  and  $\text{Al}_8\text{Co}_{17}\text{Cr}_{17}\text{Cu}_8\text{Fe}_{17}\text{Ni}_{33}$  alloys were prepared in a vacuum induction furnace. The alloy constituents were of 99.99% purity. In the following, the  $\text{Al}_{23}\text{Co}_{15}\text{Cr}_{23}\text{Cu}_8\text{Fe}_{15}\text{Ni}_{16}$  alloy will be called “the Al-rich alloy” and the  $\text{Al}_8\text{Co}_{17}\text{Cr}_{17}\text{Cu}_8\text{Fe}_{17}\text{Ni}_{33}$  alloy will be called “the Al-poor alloy”. The ingots were remelted at least three times to achieve a better homogenization. Specimens for XRD analysis and SEM observations were mechanically grinded and polished down to 50 nm using an OP-U colloidal silica suspension. XRD measurements were carried out with a Philips Expert diffractometer and with a Seifert 3000P diffractometer, both set up in Bragg–Brentano geometry with a germanium monochromator placed in the primary beam in order to provide  $\text{K}\alpha 1$  radiation of Cu only. Microstructures were characterized by SEM (ZEISS 1540 EsB crossbeam<sup>®</sup>) equipped with an energy dispersive X-ray (EDX) spectrometer.

The 3D morphology of Cu-rich phases within the  $\text{Al}_{23}\text{Co}_{15}\text{Cr}_{23}\text{Cu}_8\text{Fe}_{15}\text{Ni}_{16}$  alloy has been visualized by FIB tomography. FIB serial sectioning was performed using 30 keV Ga ions with an ion beam current of 50 pA corresponding to a milling step in z-direction of about 13 nm. SEM Imaging of 2D slices was carried out by a secondary electron (SE) detector using an acceleration voltage of 30 kV. The 3D microstructure of Cu-rich phases was visualized with the software “VGStudio MAX 2.1”.

Specimens for TEM observations were prepared in two steps, first by mechanical thinning down to a thickness of 10  $\mu\text{m}$  using a T-tool [15] and then by Ar-ion milling down to a thickness of electron transparency. Suitable samples were investigated in a TEM, Philips CM30, operated at 300 kV. The chemical composition of the different phases has been measured by a TEM/EDX spectrometer. The beam size used for TEM/EDX measurements was 10 nm.

Rods of  $0.25 \times 0.25 \times 10 \text{ mm}^3$  dimensions were cut from the ingots for 3D-AP analysis. In case of the  $\text{Al}_{23}\text{Co}_{15}\text{Cr}_{23}\text{Cu}_8\text{Fe}_{15}\text{Ni}_{16}$  alloy, the rods were considerably shorter because of the brittleness of the material. Sharp tips were prepared first by mechanical polishing down to a tip radius of around 2  $\mu\text{m}$ , using 6  $\mu\text{m}$  and then 1  $\mu\text{m}$  diamond paper followed by focused ion beam (FIB) to a tip radius of about 50 nm. For the final tip preparation an annular milling with 30 kV gallium ions and different beam currents, starting with 2 nA and finishing with 10 pA, was applied.

A 3D-AP (TAP, CAMECA) was used for the microchemical analysis of 17 samples. The measurements were carried out at a temperature of about 70 K with a pulse voltage to standing sample voltage of 0.2 and a pulse penetration frequency of 1000 Hz in a vacuum of better than  $10^{-7}$  Pa.

Vickers microhardness (HV) measurements were carried out using a load of  $\sim 2 \text{ N}$  (0.2 kp) during 10 s using a Reichert–Jung MHT-10 microhardness tester.

The software Thermo-Calc based on the CALPHAD method [14] in conjunction with the TTNi7 thermodynamic database [16] is used for calculations of the equilibrium phases as functions of the temperature.

## 3. Results

The investigated alloys have first been observed by light microscope, where both of them show very large elongated grains with dimensions up to 1 mm in length and 200  $\mu\text{m}$  in width (not shown here). Fast cooling on the water cooled copper hearth in the arc furnace results in dendritic solidification of the alloys in all cases. The as-cast Al-rich alloy has an average micro-hardness of  $\sim 580 \text{ HV}$  and the as-cast Al-poor alloy has  $\sim 280 \text{ HV}$ .

### 3.1. $\text{Al}_{23}\text{Co}_{15}\text{Cr}_{23}\text{Cu}_8\text{Fe}_{15}\text{Ni}_{16}$

The XRD spectrum of the as-cast Al-rich alloy shown in Fig. 1 indicates the presence of an ordered bcc phase with B2 structure and a lattice parameter  $a = 0.2885 \text{ nm}$ . However, SEM investigations of the Al-rich alloy show the presence of at least three phases as displayed in Fig. 2. The bright imaged precipitates are needle-like in this two dimensional representation with a length of 50–400 nm. The precipitates with light grey contrast are of plate-like or square morphology in two dimensions with an edge length of 100 nm to  $>1 \mu\text{m}$ . Precipitates located at the grain boundaries with the same light grey contrast can achieve a length of several tens of micrometers. The matrix is imaged dark grey. EDX measurements show that the phase with the light grey contrast is Fe–Cr-rich, the bright precipitates are Cu-rich and the matrix is

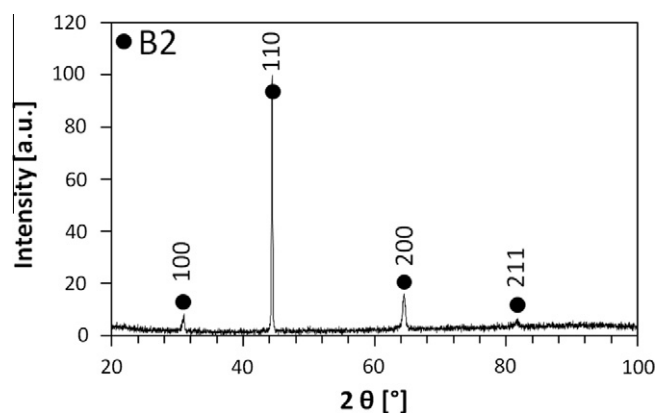


Fig. 1. XRD spectrum of  $\text{Al}_{23}\text{Co}_{15}\text{Cr}_{23}\text{Cu}_8\text{Fe}_{15}\text{Ni}_{16}$  as-cast high entropy alloy, recorded using the radiation of Cu  $\text{K}\alpha 1$ . The peaks correspond to a bcc phase with a B2 structure.

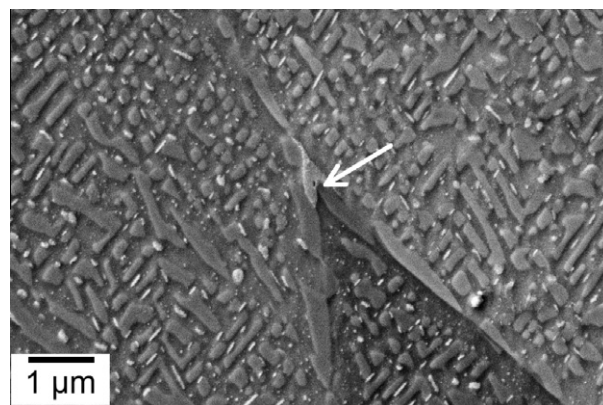
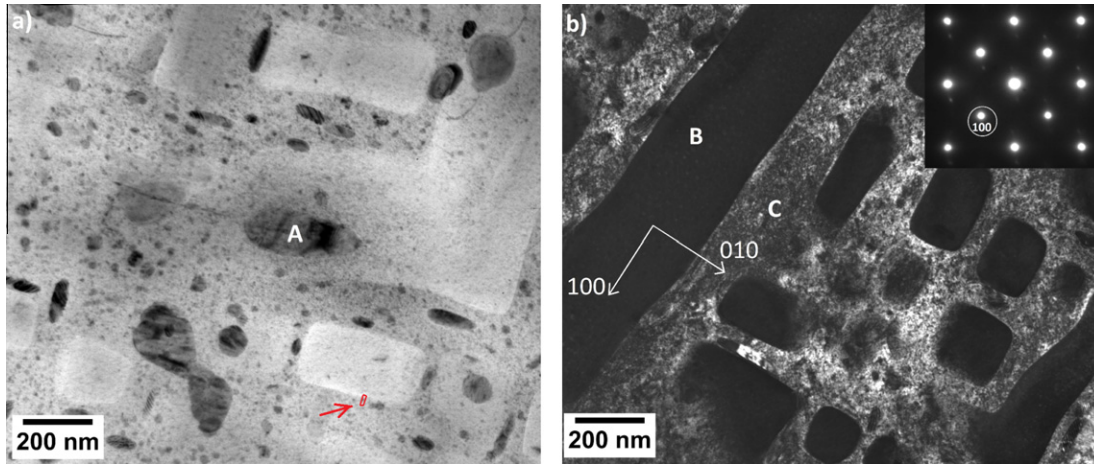


Fig. 2. SEM micrograph of the  $\text{Al}_{23}\text{Co}_{15}\text{Cr}_{23}\text{Cu}_8\text{Fe}_{15}\text{Ni}_{16}$  high entropy alloy imaged using a secondary electron detector (InLens) at 5 kV. The triple point of the grain boundaries is marked by an arrow.

Al–Ni-rich. The microstructure in Fig. 2 (the region marked by an arrow) shows a triple point of grain boundaries, which are most often characterized by the presence of long, Fe–Cr-rich phases, alternated sometimes by Cu-rich precipitates.

The bright field (BF) TEM micrograph in Fig. 3a displays a typical microstructure with several precipitates embedded in the matrix. The dark imaged precipitates indicated by A are Cu-rich. They are of different morphologies and sizes. The microstructure in the dark field (DF) TEM micrograph imaged by a [100] superlattice reflection in the [001] zone axis illustrated in Fig. 3b is dominated by two alternating phases, one being square or rectangle shaped Fe–Cr-rich precipitates, indicated by B, and an Al–Ni-rich matrix indicated by C. The Al–Ni-rich matrix is imaged bright and has therefore an ordered bcc structure, namely B2. In contrast the Fe–Cr-rich precipitates are imaged dark by the same [100] superlattice reflection and are therefore a disordered bcc phase of A2 structure. The Fe–Cr-rich precipitates, as well as the Cu-rich platelets, are aligned along the  $\langle 100 \rangle$  matrix direction. The corresponding diffraction pattern with the [001] zone axis, shown in the inset, indicates strong superlattice reflections generated by the B2 structure of the Al–Ni-rich matrix. A rectangular box at an Al–Ni/Fe–Cr interface shows the place where the sample for the later presented 3D-AP investigation could have been taken.

A three dimensional distribution of the Cu-rich precipitates with different sizes and morphologies is shown in Fig. 4. The reconstruction of an investigated volume of  $1.5 \times 1.5 \times 2.0 \mu\text{m}^3$  has been obtained by FIB tomography. A grain boundary with two large



**Fig. 3.** (a) BF TEM image showing the microstructure of the as-cast  $\text{Al}_{23}\text{Co}_{15}\text{Cr}_{23}\text{Cu}_8\text{Fe}_{15}\text{Ni}_{16}$  alloy. Dark imaged precipitates (marked by A) are Cu-rich. The rectangle shows a place where the tip for 3D-AP investigation could have been taken. (b) DF TEM micrograph of the microstructure imaged with the (100) superlattice reflection showing regions with different contrast. Dark imaged precipitates (marked by B) are Fe–Cr-rich. The inset displays the corresponding diffraction pattern with a [00 1] zone axis of the Al–Ni-rich matrix (marked by C).

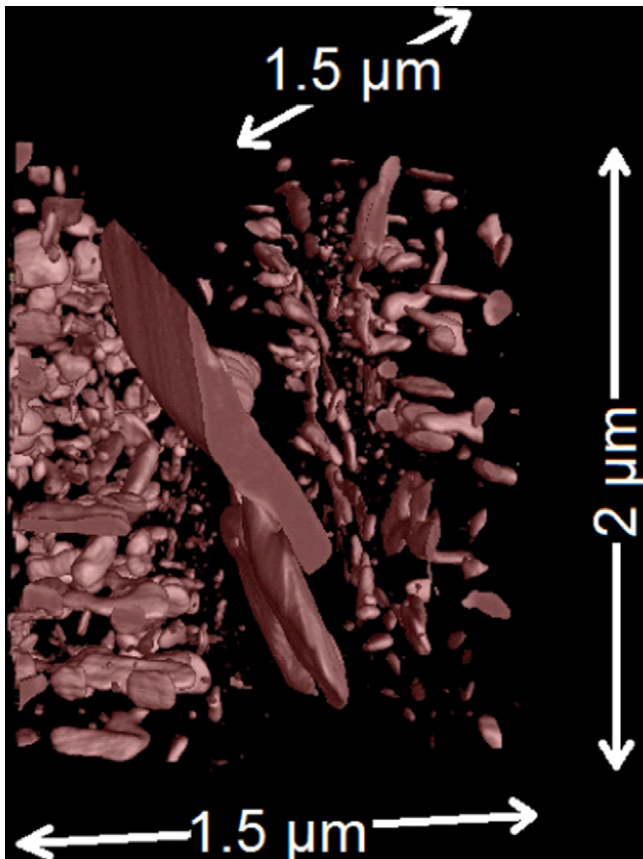


**Fig. 4.** Cu-rich precipitates with different sizes and morphologies in an investigated volume of  $1.5 \times 1.5 \times 2.0 \mu\text{m}^3$  of the as-cast  $\text{Al}_{23}\text{Co}_{15}\text{Cr}_{23}\text{Cu}_8\text{Fe}_{15}\text{Ni}_{16}$  alloy are visualized by FIB tomography. The reconstruction shows a grain boundary in the middle part, indicated by two large Cu precipitates.

plate-like precipitates can be distinguished in the middle of the selected volume. The area along the grain boundary is clearly depleted of the small spherical Cu-rich precipitates. It has been observed that the plate-like Cu-rich precipitates of smaller size are oriented perpendicularly to each other.

In order to obtain chemical information on the nanoscale level, several specimens have been investigated by 3D-AP. Fig. 5a shows

the 3D reconstruction of the atom positions of Al, Cr, Cu, Fe, Co and Ni in an investigated volume of  $14 \times 14 \times 30 \text{ nm}^3$ . All alloying elements are distributed non-uniformly. Some correlation between Al and Ni, Fe and Cr are visible. Several very thin Cu-rich plates can also be observed. The microchemical information of the enriched phases has been obtained by concentration profiles taken in a cylinder of 1 nm radius (see Fig. 5a) oriented perpendicularly to the small Cu-rich platelets. The corresponding concentration depth profiles of all elements are shown in Fig. 5b. The depth of 30 nm is subdivided in different regions which are assigned to four major compositions labelled by 1–4. While region 1 is Fe–Cr-rich, regions 2 and 4 are Cu-rich, but with different amounts of Cu, and region 3 is enriched in Al and Ni. Some of the Cu-rich precipitates observed here are only 1–2 nm wide. Because of their sizes, the composition of each precipitate has been calculated separately in order to position the cylinder (not shown here) perpendicularly to the plate-like surface of each precipitate. Even if their composition varies from one platelet to another, the Cu-rich precipitates were sorted into two types. The compositions of all regions obtained by 3D-AP measurements together with TEM/EDX analysis are listed in Table 1. The error bars for the chemical composition of the elements are represented by the standard deviation  $2\sigma$  and have been determined by standard counting statistics.

### 3.2. $\text{Al}_8\text{Co}_{17}\text{Cr}_{17}\text{Cu}_8\text{Fe}_{17}\text{Ni}_{33}$

Fig. 6 shows an XRD spectrum of the as-cast Al-poor alloy. The peaks belong mainly to an fcc phase with a lattice parameter  $a = 0.3582 \text{ nm}$ .

Investigations with SEM and TEM show a very homogeneous microstructure with up to  $700 \mu\text{m}$  long and  $100 \mu\text{m}$  wide grains (not shown here). No phases can be differentiated inside the grains. SEM/EDX and TEM/EDX investigations have been performed inside the grains and both show a homogeneous distribution of the elements. Only at the grain boundaries some very few, about 250 nm sized precipitates can be distinguished in the SEM (not shown here). SEM/EDX investigations indicate that this kind of precipitate is mainly enriched in Cu, Al, Ni and Co and depleted in Cr and Fe. Their composition is given in Table 2. The results obtained by SEM/EDX have been added only for qualitative comparison and must not be taken quantitatively because of the higher uncertainty of the method.

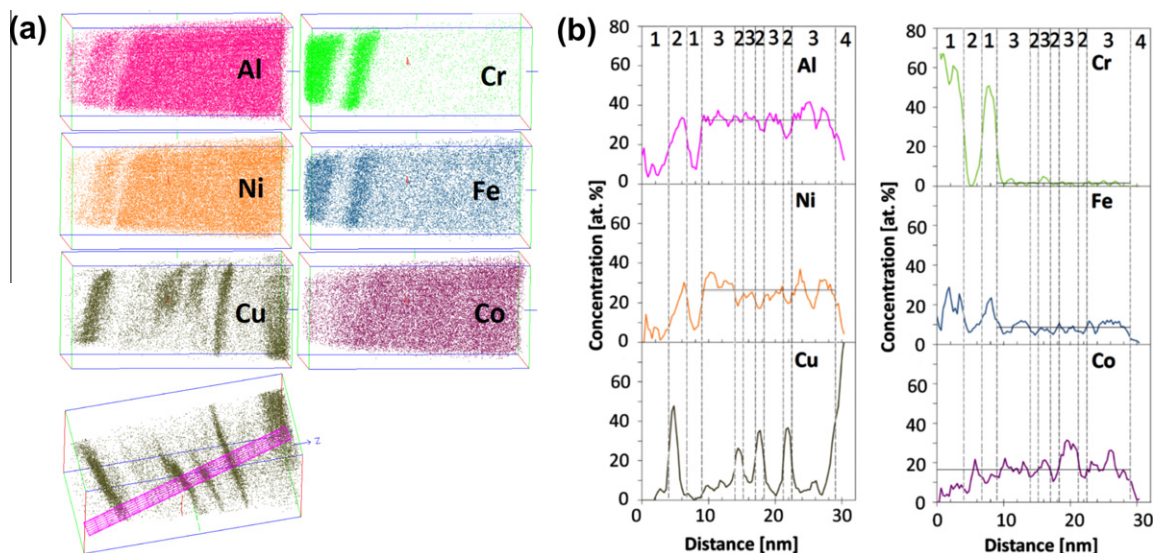


**Fig. 5.** (a) 3D reconstruction of Al, Co, Cr, Cu, Fe and Ni atom positions in an investigated volume of  $14 \times 14 \times 30 \text{ nm}^3$  of the  $\text{Al}_{23}\text{Co}_{15}\text{Cr}_{23}\text{Cu}_8\text{Fe}_{15}\text{Ni}_{16}$  as-cast alloy. (b) Concentration depth profiles of all alloying elements taken along the cylinder shown in Fig. 5a. The numbers at the top of the figure display the four different regions corresponding to the areas labelled from 1 to 4 enriched in: (1) Fe and Cr, (2) Cu, (3) Al and Ni, (4) Cu.

**Table 1**

Compositions (in at.%) of the phases in  $\text{Al}_{23}\text{Co}_{15}\text{Cr}_{23}\text{Cu}_8\text{Fe}_{15}\text{Ni}_{16}$  measured by TEM-EDX and 3D-AP compared with equilibrium phases predicted by Thermo-Calc using the CALPHAD method with the TTNi7 database. The error bars correspond to the standard deviation  $2\sigma$ .

Method	Denomination in text or figures, respectively	Al	Co	Cr	Cu	Fe	Ni
TEM-EDX	C or Al-Ni-rich B2 matrix	$28.9 \pm 1.5$	$21.2 \pm 1.1$	$10.3 \pm 3.1$	$6.1 \pm 0.4$	$12.6 \pm 1.1$	$20.8 \pm 1.3$
	B or Fe-Cr-rich A2	$3.8 \pm 0.3$	$13.3 \pm 1.1$	$50.1 \pm 3.0$	$2.3 \pm 0.9$	$26.0 \pm 0.9$	$4.6 \pm 1.6$
3D-AP	A or Cu-rich platelets	$9.4 \pm 0.5$	$2.9 \pm 0.5$	$3.8 \pm 2.6$	$76.1 \pm 4.5$	$2.8 \pm 1.3$	$5.2 \pm 0.6$
	3 or Al-Ni-rich	$34.9 \pm 3.6$	$19.3 \pm 0.8$	$2.5 \pm 1.5$	$5.7 \pm 2.4$	$9.9 \pm 1.1$	$27.5 \pm 2.3$
	1 or Fe-Cr-rich	$10.1 \pm 3.0$	$7.1 \pm 2.2$	$53.5 \pm 6.1$	$1.6 \pm 1.2$	$21.7 \pm 2.0$	$5.2 \pm 1.8$
	2 or Cu-rich	$25.5 \pm 5.4$	$8.2 \pm 3.5$	$1.7 \pm 2.3$	$46.6 \pm 12.8$	$4.2 \pm 1.8$	$13.9 \pm 5.2$
Thermo-Calc $T = 1273 \text{ K}$	4 or Cu-rich	$13.2 \pm 3.3$	$1.8 \pm 0.1$	$0.3 \pm 0.1$	$79.6 \pm 6.4$	$1.1 \pm 0.3$	$4.0 \pm 3.0$
	NiAl	37.4	18.7	3.5	4.4	8.0	28.0
	BCC-1	6.4	11.1	52.7	0.6	26.5	2.7
	FCC	10.3	9.7	0.8	74.5	1.9	3.0
Thermo-Calc $T = 973 \text{ K}$	NiAl	40.9	20.7	1.8	2.3	5.7	28.7
	BCC-1	1.2	3.1	74.2	0.0	21.4	0.1
	FCC	7.3	5.4	0.0	86.0	0.4	0.9
	$\sigma$	0.0	9.2	57.7	0.0	32.6	0.7
Thermo-Calc $T = 400 \text{ K}$	NiAl	46.0	17.9	0.0	0.2	3.7	32.2
	BCC-1	0.0	0.0	100.0	0.0	0.0	0.0
	FCC	1.2	0.5	0.0	98.3	0.0	0.0
	BCC-2	0.2	31.5	0.0	0.0	68.3	0.0

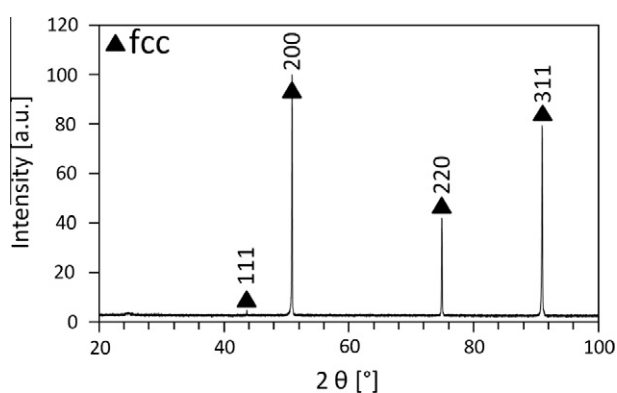


**Fig. 6.** XRD spectrum of  $\text{Al}_8\text{Co}_{17}\text{Cr}_{17}\text{Cu}_8\text{Fe}_{17}\text{Ni}_{33}$  as-cast alloy, recorded using the radiation of Cu  $K\text{-}\alpha_1$ . The pattern shows an fcc phase with  $a = 0.3586 \text{ nm}$ .

However, on a nanometre scale, the microstructure exhibits decomposed areas as can be seen in Fig. 7a, which has been obtained by DF TEM imaging of a (100) superlattice reflection in a

[001] zone axis. The diffraction pattern of the [001] zone axis is shown in the inset in Fig. 7a. The presence of forbidden spots in the diffraction pattern proves the presence of an ordered fcc phase with  $L1_2$  structure. Spherical areas with bright contrast and with sizes of less than 20 nm in diameter are visible in the DF TEM image. A rectangular box shows the place where the sample for the 3D-AP investigation could have been taken. The latter shows another example of decomposed areas within the microstructure with nearly atomic resolution (Fig. 7b). A three dimensional reconstruction of the atom positions of Al, Co, Cr, Cu, Fe and Ni is presented in an investigated volume of  $9.4 \times 9.4 \times 11.5 \text{ nm}^3$ . In the same volume, clusters enriched in Al and Ni are highlighted in pink and orange, respectively. They were calculated with a cluster-search module which has been developed by the FIM group in Rouen [17]. The concentration threshold for Ni for the calculation of the clusters was  $\geq 42\%$ , whereas the concentration threshold for Al for the matrix was  $\leq 38\%$ . This figure represents only a part of the complete experimental data. The composition of these clusters as well as the composition of the matrix measured by 3D-AP analysis is also given in Table 2.

**Table 2**  
Compositions (in at.%) of the phases in  $\text{Al}_8\text{Co}_{17}\text{Cr}_{17}\text{Cu}_8\text{Fe}_{17}\text{Ni}_{33}$  measured by SEM–EDX and 3D-AP compared with equilibrium phases predicted by Thermo-Calc using the CALPHAD method with the TTNi7 database. The error bars correspond to the standard deviation  $2\sigma$ .

Method	Denomination in the text or figures, respectively	Al	Co	Cr	Cu	Fe	Ni
SEM–EDX	Cu-rich at grain boundaries	$12.7 \pm 0.8$	$13.4 \pm 3.8$	$5.8 \pm 1.9$	$21.0 \pm 1.7$	$9.9 \pm 2.3$	$37.1 \pm 1.3$
3D-AP	Matrix	$7.1 \pm 0.7$	$19.0 \pm 1.1$	$19.5 \pm 1.1$	$3.1 \pm 0.5$	$19.4 \pm 1.1$	$31.8 \pm 1.3$
	Ni–Al-rich	$11.5 \pm 1.0$	$14.0 \pm 2.9$	$8.6 \pm 1.6$	$6.1 \pm 1.7$	$12.6 \pm 1.4$	$47.1 \pm 5.0$
Thermo-Calc $T = 1273$ K	FCC-2	8.0	17.0	17.0	8.0	17.0	33.0
Thermo-Calc $T = 973$ K	FCC-2	5.0	18.4	19.9	4.4	19.7	32.5
	NiAl	32.8	8.6	3.4	2.1	5.6	47.5
	FCC-1	3.1	13.1	0.2	75.4	0.6	7.6
	$\gamma'$ -1	21.3	7.7	5.1	12.8	2.1	51.0
Thermo-Calc $T = 600$ K	FCC-1	0.0	10.7	0.0	84.5	0.0	4.8
	$\gamma'$ -1	19.2	2.1	5.1	1.2	1.7	70.7
	BCC-1	0.0	0.4	98.9	0.0	0.7	0.0
	BCC-2	0.0	46.6	0.5	0.0	51.1	1.8
	FCC-3	0.3	29.4	0.0	2.9	25.9	41.4
Thermo-Calc $T = 400$ K	FCC-1	0.0	3.8	0.0	95.1	0.0	1.1
	$\gamma'$ -1	22.3	0.3	2.7	0.5	0.0	74.2
	BCC-1	0.0	0.0	100.0	0.0	0.0	0.0
	BCC-2	0.0	52.7	0.0	0.0	47.1	0.2
	$\gamma'$ -2	0.0	0.3	0.4	0.0	25.4	73.8

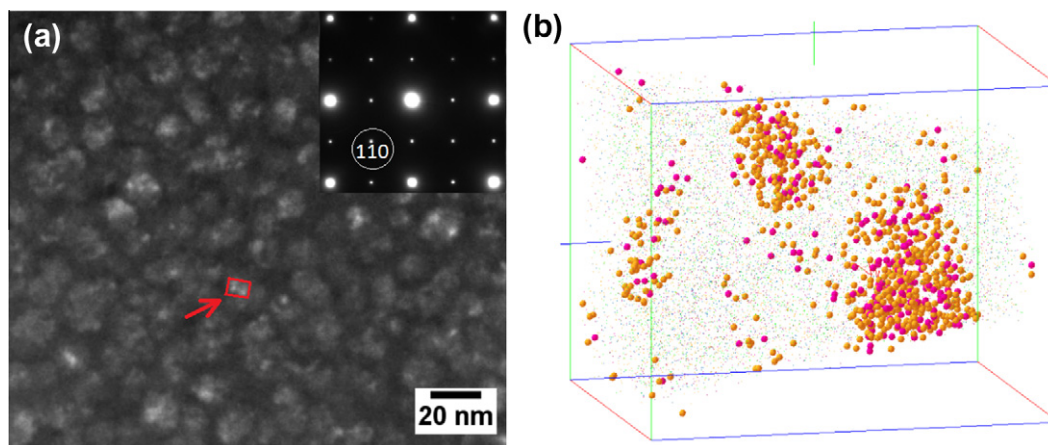


**Fig. 7.** (a) DF TEM image of the microstructure of the  $\text{Al}_8\text{Co}_{17}\text{Cr}_{17}\text{Cu}_8\text{Fe}_{17}\text{Ni}_{33}$  alloy and the corresponding diffraction pattern of the [001] zone axis in the inset. The rectangle shows a place where the tip for 3D-AP investigation could have been taken (b) 3D reconstruction of Al, Co, Cr, Cu, Fe and Ni atom positions in an investigated volume of  $9.4 \times 9.4 \times 11.5 \text{ nm}^3$  of the  $\text{Al}_8\text{Co}_{17}\text{Cr}_{17}\text{Cu}_8\text{Fe}_{17}\text{Ni}_{33}$  alloy. Clusters enriched in Ni and Al (threshold for Al clusters  $\geq 12\%$ ) are also highlighted in the same volume. They were calculated with a cluster-search module developed by the FIM group in Rouen [17].

#### 4. Discussion

It is obvious that slight composition changes of AlCoCrCuFeNi high entropy alloys may have a strong influence on phase formation. Higher amounts of Al and Cr in the Al-rich alloy enhance the formation of bcc phases (Fig. 1) whereas a higher amount of Ni in the Al-poor  $\text{Al}_8\text{Co}_{17}\text{Cr}_{17}\text{Cu}_8\text{Fe}_{17}\text{Ni}_{33}$  alloy enhances the formation of fcc phases (Fig. 6). The present results are in good agreement with observations reported previously [4,5,10].

The microstructure of the Al-rich alloy is similar to that of the equiatomic AlCoCrCuFeNi alloy [4,5,10,18] with Fe–Cr-rich and several Cu-rich precipitates embedded in the Al–Ni-rich matrix. The structure of the Cu-rich precipitates could not be determined at present. Plate-like Cu-precipitates in equiatomic AlCoCrCuFeNi have a cubic structure according to Singh et al. [10]. 3D-AP analysis proved different compositions in all four Cu-rich platelets shown in Fig. 5. The deviation in composition can be explained either by their small thickness of only a few interplanar distances and the uncertainty of measurements or by the presence of a large range of existence of this kind of Cu-rich precipitates. Large fluctuations of Cr observed in Fe–Cr-rich regions (not shown here) are due to spinodal decomposition in this alloy. The latter has also been reported for the equiatomic alloy [8].

Thermodynamic calculation offers a means by which phase equilibrium in multi-component alloys can be predicted. Quantification of phase constitution and element distribution in the phases is also attempted. The calculated equilibrium phases with their chemical composition are compared with those experimentally obtained by atom probe microanalysis and TEM/EDX. The calculated equilibrium phase diagram for the Al-rich alloy is shown in Fig. 8a. According to the Thermo-Calc calculations the melt solidifies eutectically into the two phases NiAl and BCC-1, which correspond to the Al–Ni rich and the Fe–Cr rich phases, respectively, which have been found experimentally. Phase compositions determined by different methods are listed in Table 1. However, discrepancies in the composition of constituencies between theoretical and experimental values are clearly visible. The phases measured in the current work have not reached the calculated equilibrium composition, which is due to thermodynamic and kinetic reasons. The compositions of both phases numbered B and 1 are Fe–Cr-rich and very close, the small differences being due to the high absorption of Al during EDX measurements and the fact that Fe, Co and Ni have very close ordering numbers. In the following B and 1 will be treated as one phase. Apart from the experimentally observed Al–Ni-rich, Fe–Cr-rich and Cu-rich phases the Thermo-Calc calculation predicts at a temperature

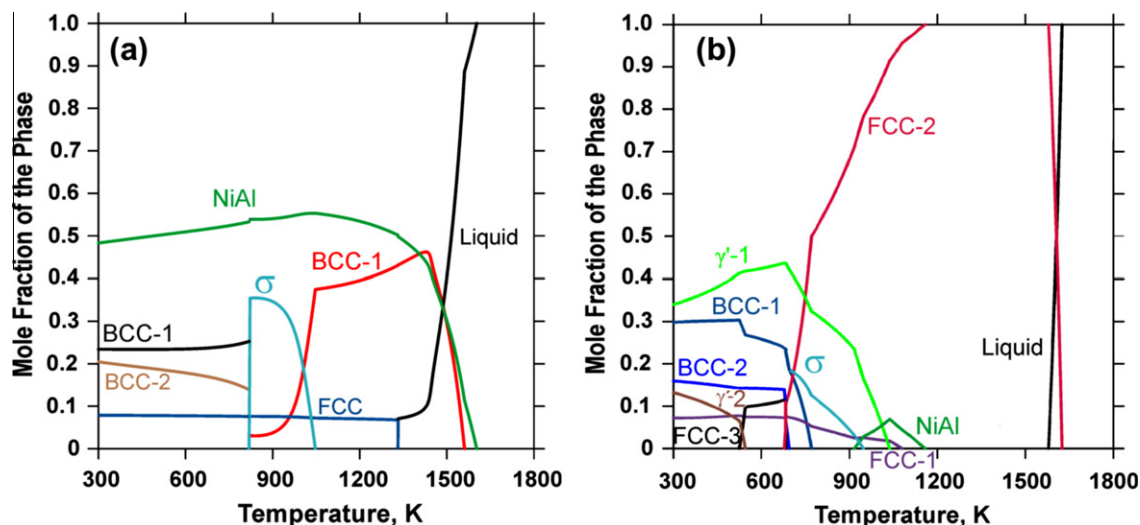


Fig. 8. Thermo-Calc calculation diagrams, calculated using the CALPHAD method with the TTNi7 database, for (a) the  $\text{Al}_{23}\text{Co}_{15}\text{Cr}_{23}\text{Cu}_8\text{Fe}_{15}\text{Ni}_{16}$  alloy and (b) the  $\text{Al}_8\text{Co}_{17}\text{Cr}_{17}\text{Cu}_8\text{Fe}_{17}\text{Ni}_{33}$  alloy.

range from about 800 to 1050 K the formation of another phase named “sigma”, which could not be observed experimentally. This is probably due to a high solidification rate, which inhibits the phase’s precipitation. The high temperature phase NiAl and BCC-1 remain in a metastable state. The only stable phase that forms during cooling is the Cu-rich fcc phase.

The volume fraction for each phase in the Al-rich alloy was estimated by making use of mass conservation and the lever-rule [19], which is usually used for atom probe measurements. By using the compositions determined by 3D-AP it can be calculated that the volume fraction of the Fe–Cr-rich phase is  $f_{\text{Fe-Cr}} \approx 43\%$ , while  $f_{\text{Al-Ni}} \approx 46\%$  and  $f_{\text{Cu}} \approx 6\%$ . The volume fraction of the two main phases, Al–Ni-rich and Fe–Cr-rich, is very close. The volume fractions of phases estimated from 3D-AP measurements are also in good agreement with those calculated by Thermo-Calc.

The microstructure of the Al-poor alloy is different from that of the equiatomic  $\text{AlCoCrCuFeNi}$  [4,5,10,18] and of the Al-rich alloy. A number of phases appear in equilibrium in the Al-poor alloy when all the phases are included in the calculation as shown in Table 2 and Fig. 8b. The dominant phases in the Al-poor alloy measured by XRD and TEM are phases with an fcc structure. However, several equilibrium phases calculated by Thermo-Calc form a bcc structure (see Table 2), which could not be supported neither by 3D-AP nor TEM analysis. The presence of Ni-rich phases of two different compositions is supported by TEM and 3D-AP results, one of their compositions being listed in Table 2. The second phase seems to form around the tiny  $\text{Ni}_3\text{Al}$  spheres, as can be seen in Fig. 7. Its composition can, however, not be determined by 3D-AP because the interfaces between the phases are not sharp enough. The increase of the Ni content in the Al-poor alloy causes the formation of an fcc ordered phase with a  $L1_2$  structure of  $\text{Ni}_3\text{Al}$  type ( $\gamma'$  phase). However, the chemical composition of Ni-rich phases obtained in the present study is far from the stoichiometric composition predicted by Thermo-Calc. The Ni–Al-rich clusters were found to contain about 47 at.% Ni and about 11 at.% Al by 3D-AP analysis. The substitution of Ni atoms by Co and Cr (whose combined percentage is about 23 at.%) in the  $\gamma'$  phase is possible according to a previous study of Ni-based superalloys [20,21]. It has been shown that Cr and Co clearly prefer Ni-sites within the  $\gamma'$  phase [17,18]. Most probably the element Fe preferably takes up the Al sites. The formation of an fcc matrix depleted in Al and Cu (Table 2) was also

predicted by Thermo-Calc calculation. The phase enriched in Cu could only be measured by SEM/EDX. The composition of this phase is listed in Table 2 under “Cu-rich at grain boundaries”. Since the beam spot size in the SEM was too large, the composition therefore consists not only of Cu but of all alloying elements. The equilibrium  $\gamma'$  phase enriched with Ni and Fe and the bcc phase enriched with Cr, both shown in Table 2 (phases  $\gamma'-2$  and BCC-2, respectively) could not be observed.

The volume fraction of phases in the Al-poor alloy could not be determined properly since within the individual globular areas shown in Fig. 8a, the fluctuations in composition are too large.

The number of phases and their composition found in the Al-rich alloy are in good agreement with the equilibrium phases predicted by Thermo-Calc, unlike in the Al-poor alloy, where there are significant discrepancies when comparing the number of phases. Such discrepancies between the calculated and the experimental data occur most probably because the samples did not reach equilibrium during the cooling down from the melt. A necessary prerequisite to compare experiments with Thermo-Calc would be proper long time annealing at defined temperatures.

## 5. Summary

- The  $\text{Al}_8\text{Co}_{17}\text{Cr}_{17}\text{Cu}_8\text{Fe}_{17}\text{Ni}_{33}$  and  $\text{Al}_{23}\text{Co}_{15}\text{Cr}_{23}\text{Cu}_8\text{Fe}_{15}\text{Ni}_{16}$  high entropy alloys have been investigated by SEM, TEM, XRD and 3D atom probe.
- The brittle  $\text{Al}_{23}\text{Co}_{15}\text{Cr}_{23}\text{Cu}_8\text{Fe}_{15}\text{Ni}_{16}$  alloy shows formation of three types of phases, namely an Al–Ni-rich matrix whose volume fraction as estimated from the 3D-AP analysis is  $\sim 46\%$ , Fe–Cr-rich cubes and parallelepipeds whose volume fraction is  $\sim 43\%$ , and Cu-rich precipitates (platelets at grain boundaries and spherical precipitates inside the Al–Ni-rich phase) whose fraction is  $\sim 6\%$ . The Al–Ni- and Fe–Cr-rich phases are found to be coherent.
- The ductile  $\text{Al}_8\text{Co}_{17}\text{Cr}_{17}\text{Cu}_8\text{Fe}_{17}\text{Ni}_{33}$  alloy shows mainly two fcc phase in TEM, one of them being a Ni–Al-rich ordered phase of  $L1_2$  structure and the other being a disordered fcc matrix. However, several fluctuations with different compositions were measured by 3D-AP. Very few Cu-rich precipitates are observed at the grain boundaries.

- Whereas the formation of phases in the  $\text{Al}_{23}\text{Co}_{15}\text{Cr}_{23}\text{Cu}_8\text{Fe}_{15}\text{Ni}_{16}$  alloy corresponds to the predicted equilibrium phases by Thermo-Calc calculation, the formation of phases in the  $\text{Al}_8\text{Co}_{17}\text{Cr}_{17}\text{Cu}_8\text{Fe}_{17}\text{Ni}_{33}$  alloy corresponds only partially to the predicted ones.

### Acknowledgements

The authors are grateful to the German Research foundation (DFG) for the financial support by WA 1378/15-1 and GL 181/25-1. The authors would like to thank C. Förster for sample preparation and H. Kropf for help with FIB-tomography.

### References

- [1] S. Ranganathan, *Curr. Sci.* 85 (2003) 1404.
- [2] J.W. Yeh, *Knowl. Bridge* 40 (2003) 1.
- [3] J.W. Yeh, S.K. Che, S.J. Lin, J.Y. Gan, T.S. Chin, T.T. Shun, C.H. Tsau, S.Y. Chang, *Adv. Eng. Mater.* 6 (2004) 299.
- [4] C.C. Tung, J.W. Yeh, T.T. Shun, S.K. Chen, Y.S. Huang, H.C. Chen, *Mater. Lett.* 61 (2007) 1.
- [5] C.J. Tong, Y.L. Chen, S.K. Chen, J.W. Yeh, T.T. Shun, C.H. Tsau, S.J. Lin, S.Y. Chang, *Metall. Mater. Trans.* 36A (2005) 881.
- [6] T.K. Chen, T.T. Shun, J.W. Yeh, M.S. Wong, *Surf. Coat. Technol.* 188 (2004) 193.
- [7] B. Cantor, I.T.H. Chang, P. Knight, A.J.B. Vincent, *Mater. Sci. Eng. A* 375 (2004) 213.
- [8] S. Singh, N. Wanderka, K. Kiefer, K. Siemensemeyer, J. Banhart, *Ultramicroscopy* 111 (2011) 619.
- [9] K.B. Zhang, Z.Y. Fu, J.Y. Zhang, J. Shi, W.M. Wang, H. Wang, Y.C. Wang, Q.J. Zhang, *J. Alloys Comp.* 502 (2010) 295.
- [10] S. Singh, N. Wanderka, B.S. Murty, U. Glatzel, J. Banhart, *Acta Mater.* 59 (2011) 182.
- [11] C.J. Tong, M.R. Chen, S.K. Chen, J.W. Yeh, T.T. Shun, S.J. Lin, S.Y. Chang, *Metall. Mater. Trans. A* 36A (2005) 1263.
- [12] F. Zhu, H. Wendt, P. Haasen, *Scr. Metall.* 16 (1982) 1175.
- [13] S.S. Brenner, M.K. Miller, W.A. Soffa, *J. Met.* 34 (1982) 34.
- [14] Thermo-Calc Ni-based Superalloys Database, TTNI7, 7.0 7.0, Thermo-Calc Software AB, Stockholm, Sweden, 2006.
- [15] P. Schubert-Bischoff, Personal Communication.
- [16] J.O. Andersson, T. Helander, L.H. Hoglund, P.F. Shi, B. Sundman, *CALPHAD* 26 (2002) 273.
- [17] X. Sauvage, G. Da Costa, R.Z. Valiev, in: Y.T. Zhu, T.G. Langdon, R.Z. Valiev, S.L. Semiatin, D.H. Shin, T.C. Lowe (Eds.), *Proceedings on Ultrafine Grained Materials III, TMS 2004 Annual Meeting*, 31pp.
- [18] Y.P. Wang, B.S. Li, H.Z. Fu, *Adv. Eng. Mater.* 11 (2009) 641.
- [19] V. Kindrachuk, *Micostructure Investigation of Modified Inconel 706 Superalloys after Different Thermal Treatments* Ph.D. Thesis, TU, Berlin, Germany, 2006.
- [20] N. Wanderka, U. Glatzel, *Mater. Sci. Eng. A* 203 (1995) 69.
- [21] C.H. Liebscher, R. Voelkl, U. Glatzel, *Acta Mater.* 57 (2009) 4217.